



Microstructure, Mechanical and Wear Resistance Properties of AlCoCrFeNi_{2.1-x}Ni₃Al Eutectic High-Entropy Alloy Matrix Composites

Li Li^{1,2} · Xiao Kong² · Hui Jiang² · Wenna Jiao³ · Di Jiang² · Jichao Ren⁴

Received: 25 April 2024 / Revised: 15 July 2024 / Accepted: 27 July 2024

© The Chinese Society for Metals (CSM) and Springer-Verlag GmbH Germany, part of Springer Nature 2024

Abstract

AlCoCrFeNi_{2.1-x}Ni₃Al ($x=0, 5.0, 7.5,$ and 10 wt%, denoted as Ni₃Al₀, Ni₃Al_{5.0}, Ni₃Al_{7.5}, and Ni₃Al₁₀) eutectic high-entropy alloy (EHEA) matrix composites were fabricated by mechanical alloying and spark plasma sintering methods. The effects of Ni₃Al content on the microstructures, mechanical and wear properties of AlCoCrFeNi_{2.1} EHEA were investigated. The results indicate that the AlCoCrFeNi_{2.1-x}Ni₃Al composites present cellular grid morphologies composing of FCC/L1₂ and B2 phases, and a small amount of Al₂O₃ and Cr₇C₃ phases. The addition of Ni₃Al significantly enhanced the compressive yield strength, compressive fracture strength, compressive strain and wear properties of the AlCoCrFeNi_{2.1} composites. In particular, the Ni₃Al₁₀ composite exhibits excellent comprehensive mechanical properties. The compressive yield strength, compressive fracture strength and compressive strain of the Ni₃Al₁₀ composite, are 1845 MPa, 2301 MPa and 10.1%, respectively. The friction coefficient, wear width and depth, and mass loss of the Ni₃Al₁₀ composite were 0.40, 0.9 mm, 20.5 mm, 0.016 g, respectively. Moreover, the wear mechanism of the Ni₃Al₁₀ composite is major abrasive wear with a small amount of adhesive wear.

Keywords Eutectic high-entropy alloy composites · Microstructures · Mechanical properties · Wear properties

1 Introduction

Based on the advantages of metal matrix composites [1, 2] and high-entropy alloys (HEAs) [3–6], the high-entropy alloy matrix composites (HEAMCs) are expected to exceed the performance limits of traditional metal composites by adding reinforcement particles to HEAs [7–11]. In addition, the reinforcements particles added will directly affect the performance of the composites. Due to the low cost, high

hardness and elastic modulus, ceramic particle is usually added to the HEAs to improve strength and wear resistance of alloys, such as TiC [12], WC [13], SiC [9], NbC [10]. Whereas, the ceramic particles further improve the strength and wear resistance of alloys at the expense of plasticity for the low ductility, and it is difficult to achieve the comprehensive performance enhancement of the alloys [14]. Zheng et al. [15] introduced Ni₃Al particles into CoCrFeNi HEA to prepare CoCrFeNi(Ni₃Al)_x EHEA matrix composites. The results exhibited that the addition of the Ni₃Al obviously enhance the mechanical properties. Wherein the CoCrFeNi(Ni₃Al)₁₀ alloy has excellent comprehensive mechanical properties with yield strength of 910 MPa, fracture strength of 1200 MPa and elongation of 14%, respectively. Compared with conventional ceramic particles, the Ni₃Al with L1₂ structure as a metal particle reinforcement has some unique advantages. For example, Ni₃Al has both metallic plasticity/toughness and ceramic strength/hardness due to the presence of both metallic and covalent bonds, and exhibits good toughness; Ni₃Al has good chemical compatibility and wettability with the HEA matrix, and can form a good bonding interface; Ni–Al binary equilibrium phase diagram shows that the γ' -Ni₃Al phase is fairly stable from

Available online at <http://link.springer.com/journal/40195>.

✉ Hui Jiang
Jianghui2019@sdust.edu.cn

- 1 College of Intelligent Engineering, Taishan College of Science and Technology, Taian 271038, China
- 2 College of Mechanical and Electronic Engineering, Shandong University of Science and Technology, Qingdao 266590, China
- 3 School of Material Science and Engineering, Dalian University of Technology, Dalian 116081, China
- 4 Qingdao Kompres Energy Technology Co., Ltd, Qingdao 266073, China

room temperature to melting point temperature and does not undergo phase transformation.

Lu et al. [16] combined the concept of eutectic alloys and HEAs to proposed a new concept of eutectic high entropy alloys (EHEAs) and successfully designed and prepared the FCC(L1₂) + BCC(B2) two-phase AlCoCrFeNi_{2.1} EHEA, which exhibited a tensile fracture strength and elongation of 944 MPa and 25.6% at room temperature, respectively. With the continuous study of AlCoCrFeNi_{2.1} EHEA [17–20], it has been found that the stable structure and excellent comprehensive properties of the AlCoCrFeNi_{2.1} EHEA make it the most potential material for HEAMCs [21–27]. Moreover, multiple methods can be utilized for the fabrication of HEAMCs, including 3D printing [28, 29], atomic layer deposition [30], melt metallurgy method [31, 32], powder metallurgy [10]. Compared to other methods, the powder metallurgy technology makes powders uniform, and even form nanocrystals, which is conducive to the preparation of multi-component alloys with significant differences in element melting points, while avoiding component segregation caused by liquid solidification process.

Therefore, in this paper, Ni₃Al metal particle was selected to add into AlCoCrFeNi_{2.1} EHEA to further improve the wear resistance as well as comprehensive mechanical properties. And the AlCoCrFeNi_{2.1-x}Ni₃Al ($x=0, 5.0, 7.5$ and 10 wt%) EHEA matrix composites were prepared by powder metallurgy. The influence of Ni₃Al content on the microstructures, mechanical properties and wear properties of AlCoCrFeNi_{2.1-x}Ni₃Al alloys were explored, and the wear mechanism of the alloys were elucidated, and the relationship between the particles content and properties was established.

2 Experimental

The high purity Al, Co, Cr, Fe, and Ni powders (more than 99.9 wt%, and an average particle size of 45 μm) were employed as the AlCoCrFeNi_{2.1} EHEA powder. The Ni₃Al particles with the content of 0, 5.0, 7.5, 10 wt% (purity with 99.9 wt%, average particle size with 45 μm) were added into the AlCoCrFeNi_{2.1} powder. The powder was milled at 300 r/min for 50 h in 30 min intervals, and the ball to powder ratio was maintained at 10:1. The milled powders were subjected to spark plasma sintering furnace at 1100 °C for 15 min with an applied pressure of 50 MPa to obtain cylindrical blocks of 15 mm diameter and 11 mm height. The density of the composites was measured using the Archimedes drainage method. The phase structures were performed using X-ray diffractometer (Rigaku Ultima IV, Japan) with Cu target, voltage of 40 kV, scanning range from 20° to 100°, and scanning speed of 4°/min. The samples and wear surfaces morphology were analyzed by scanning electron

microscopy (SEM, Carl Zeiss) with an energy dispersive spectrometer (EDS). The mechanical properties of composites were examined by compression tests (MTS E45.305) using a cylindrical sample with $\Phi 5 \times 10$ mm at a strain rate of $1 \times 10^{-3} \text{ s}^{-1}$. The Vickers microhardness was measured with a Vickers hardness tester (MH-50) at a loading of 500 g and with a dwell time of 15 s. The dry wear tests were carried out on multifunctional friction and wear testing machine (Rtec MFT-5000, United States) with ball-on-disk dry sliding reciprocating friction at room temperature. The friction counterpart used Si₃N₄ ceramic ball with a size of 9.8 mm. The round trip distance, sliding speed, loads, and sliding time of tests were 5 mm, 1 Hz, 10 N, and 30 min, respectively. A three-dimensional morphometer (Contour GT-K1, Germany) was used to measure the worn volume and morphology of the tracks. The corresponding wear rates ($\text{mm}^3 \text{ N}^{-1} \text{ m}^{-1}$) were calculated by the equation: $W = V/FL$, where V is the worn volume (mm^3), F is the normal load (N) and L is the sliding distance (m).

3 Results and Discussion

3.1 Microstructures of EHEA Matrix Composites

Figure 1 shows the XRD diffraction patterns of the AlCoCrFeNi_{2.1-x}Ni₃Al EHEA matrix composites. As it can be seen, all composites are composed of both FCC/L1₂ and B2 phases, as well as a small amount of Al₂O₃ and Cr₇C₃. The L1₂ phase diffraction peak almost coincides with the FCC phase diffraction peak, and the calculated lattice constants are 0.3592 Å for FCC and 0.3572 Å for L1₂, respectively. The Ni₃Al0 and Ni₃Al5.0 composites have strong L1₂/

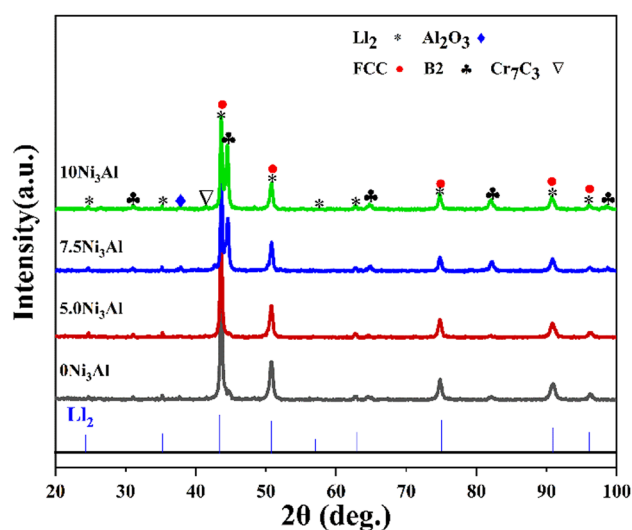


Fig. 1 XRD diffraction patterns of the AlCoCrFeNi_{2.1-x}Ni₃Al EHEA matrix composites

FCC phase diffraction peaks, and weak B2 phase diffraction peaks. With a further increase in the Ni₃Al content, the diffraction peak intensity of the B2 phase increase. When the content of Ni₃Al reaches 10 wt%, the diffraction peak intensity of the hard B2 phase and the soft Ll₂/FCC phase are almost identical, which indicates that the volume fraction of B2 phase is close to that of Ll₂/FCC phase in the Ni₃Al10 composite. This combination of phase volume fraction may be likely to balance the plasticity and strength of the Ni₃Al10 alloy.

The densities of all composites were obtained by Archimedes method, and the calculated densities of AlCoCrFeNi_{2.1-x}Ni₃Al ($x=0, 5.0, 7.5, 10$ wt%) composites were 95%, 94%, 93.5%, 95%, respectively. Besides, no pores were found to be generated from the microscopic morphology, which indicates that the AlCoCrFeNi_{2.1-x}Ni₃Al composites has a high dense microstructure.

The SEM images of the AlCoCrFeNi_{2.1-x}Ni₃Al composites are shown in Fig. 2. It can be seen from Fig. 2a, c, e and g that all composites are composed of cellular grid

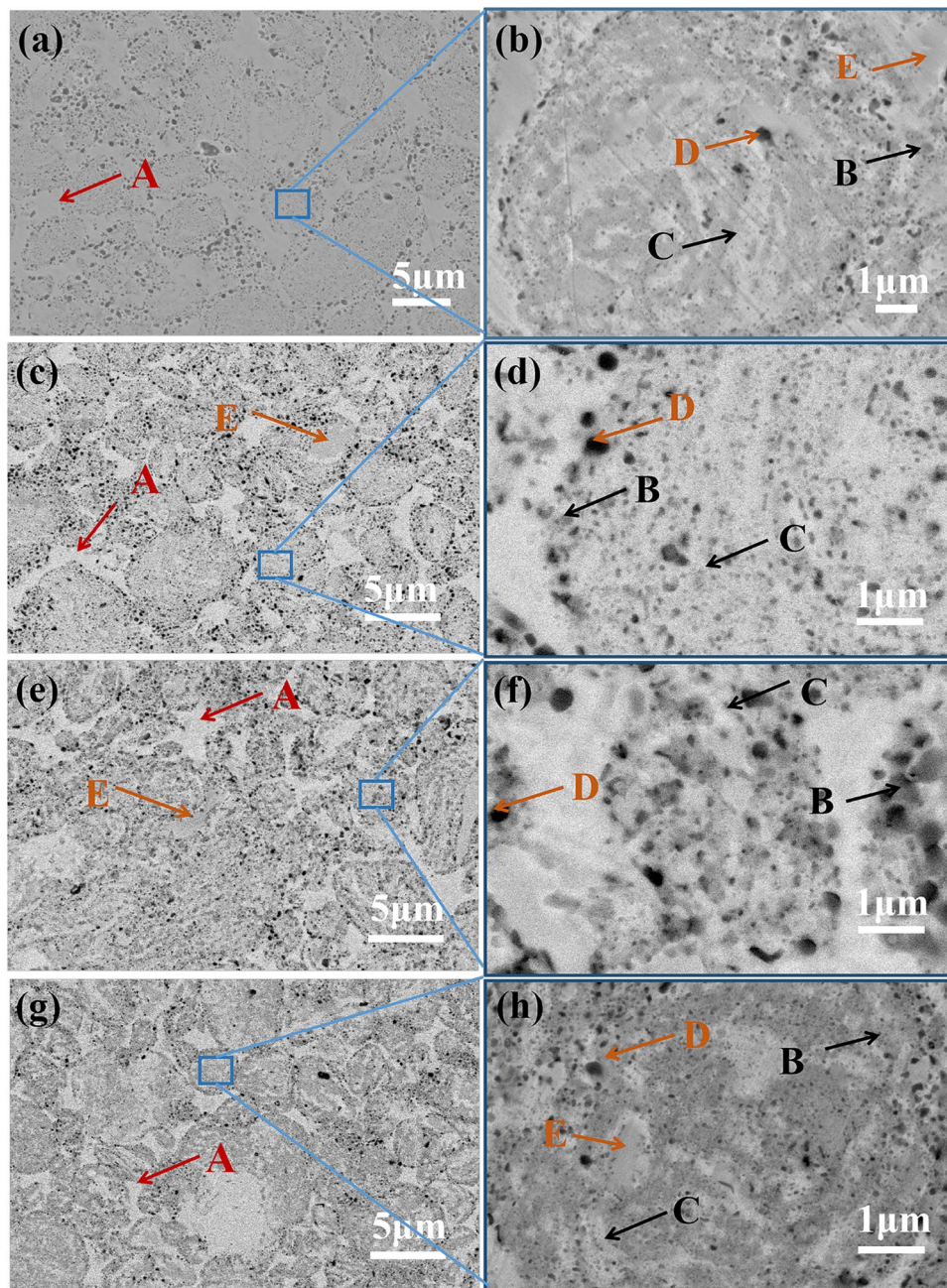


Fig. 2 SEM images of the AlCoCrFeNi_{2.1-x}Ni₃Al EHEA matrix composites: **a** and **b** $x=0$; **c** and **d** $x=5.0$; **e** and **f** $x=7.5$; **g** and **h** $x=10$

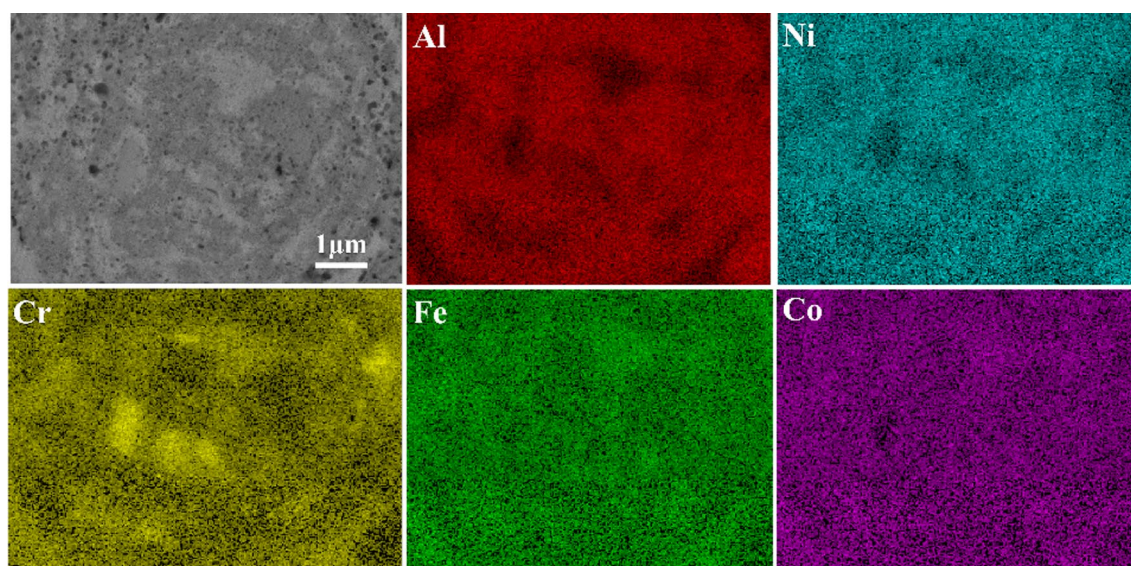
Table 1 Chemical compositions of different regions in the AlCoCrFeNi_{2.1-x}Ni₃Al EHEA matrix composites (at.%)

Alloys	Regions	Al	Co	Cr	Fe	Ni	C	O
$x=0$	A	7.78	18.82	16.69	20.68	36.03	–	–
	B	28.37	11.81	10.24	12.96	36.72	–	–
	C	15.85	17.27	16.31	18.25	32.31	–	–
	D	29.67	5.47	5.67	6.33	9.85	6.46	36.55
	E	3.07	6.98	47.28	7.37	6.94	28.36	–
$x=5.0$	A	14.57	17.46	11.69	18.39	37.89	–	–
	B	23.49	15.42	11.02	15.26	34.81	–	–
	C	10.64	19.06	17.01	21.43	31.32	–	–
	D	18.46	8.04	7.58	8.21	16.82	11.00	29.89
	E	2.21	4.60	50.02	7.81	10.81	24.55	–
$x=7.5$	A	8.89	19.07	16.57	23.75	31.72	–	–
	B	23.69	13.08	15.14	13.49	30.89	–	–
	C	13.89	17.57	15.89	18.53	34.12	–	–
	D	19.55	7.47	9.63	6.77	12.24	12.02	32.32
	E	1.05	1.77	51.17	2.73	3.26	39.05	0.99
$x=10$	A	6.94	18.09	18.96	23.60	32.41	–	–
	B	34.22	12.30	7.62	13.57	32.29	–	–
	C	16.7	18.65	17.87	19.51	27.30	–	–
	D	29.19	4.68	2.18	5.42	20.92	14.68	22.93
	E	0.22	2.38	54.08	4.41	2.27	36.09	0.55

morphologies surrounded by large gray phases (define as the A phase). The reason for the formation of this double-scale morphology is uneven powder temperature distribution during SPS. During the sintering process, the temperature on the surface of the AlCoCrFeNi_{2.1-x}Ni₃Al EHEA matrix composites powders is higher, leading to the higher grain growth rate. And the grain size is easy to form micron level on the powders surface. While the internal temperature is lower and the grain growth rate is slow, thus forming relatively fine grains. With the increase of Ni₃Al content, the volume fraction of A phase first increases and then decreases. In

addition, as shown in Fig. 2b, d, f, g, the inner part of the cellular grid is consisted of four phases (define as B, C, D, and E phases). Wherein, B and C phases with a larger volume fraction are almost alternately distributed, and the nanoscale spherical D phase is diffusely distributed. The D phase is diffusely distributed on the boundary of A phase, and E phase is randomly distributed inside the cellular grid.

The distribution of elements in different regions of AlCoCrFeNi_{2.1-x}Ni₃Al ($x=0, 5.0, 7.5$, and 10) EHEA matrix composites are given by EDS, as listed in Table 1. To more vividly describe the elements distribution in cellular grid,

**Fig. 3** EDS elemental mapping of the AlCoCrFeNi_{2.1} EHEA

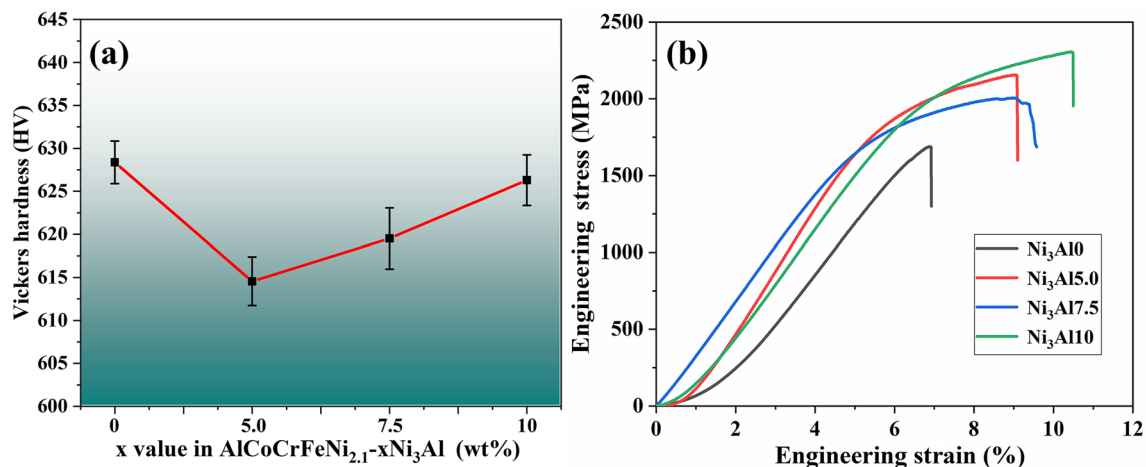


Fig. 4 **a** Vickers hardness, **b** compressive stress–strain curve at room temperature of the AlCoCrFeNi_{2.1-x}Ni₃Al EHEA matrix composites

Table 2 Mechanical properties of the AlCoCrFeNi_{2.1-x}Ni₃Al EHEA matrix composites

Alloys	Compressive yield strength, σ_y (MPa)	Compressive fracture strength, σ_{bc} (MPa)	Plastic strain, ϵ_P (%)	Vickers hardness (HV)
Ni ₃ Al0	–	1700	7.0	628
Ni ₃ Al5.0	1614	2148	8.8	611
Ni ₃ Al7.5	1722	1989	9.5	619
Ni ₃ Al10	1845	2301	10.1	626

the EDS mapping is shown in Fig. 3. It can be found that region A is enriched in Co, Cr, Fe and Ni elements, region B is enriched in Al and Ni elements, region C is enriched in Co, Cr, Fe, and Ni elements similar to region A, but the ratio of sum content of Co, Fe, and Ni elements to sum content of Al, Cr elements in region A is close to 3/1, which is the same as the Ni₃Al structure [32]. Region D is enriched in Al and O elements, and region E is enriched in Cr and C elements. Combined with the XRD and EDS results, the Co, Cr, Fe and Ni-rich region A is a Ll₂ phase, the Al, Ni-rich region B is a B2 phase, the Co, Cr, Fe and Ni-rich region C is FCC phase, the Al, O-rich region D is a Al₂O₃, and the rich Cr, C-rich region E is Cr₇C₃. Wherein, Cr₇C₃ and Al₂O₃ are produced as a result of carbon/oxygen contamination during ball milling and entrained oxygen between the graphite punch and die during sintering, and their formation also has been observed in many MA + SPS prepared alloy systems [10].

Figure 4 demonstrates the Vickers hardness and the compressive stress–strain curves at room temperature for the AlCoCrFeNi_{2.1-x}Ni₃Al EHEA matrix composites. The specific values of the compressive yield strength, compressive fracture strength, compressive strain, and Vickers hardness are listed in Table 2. As seen in Fig. 4a and

Table 2, all the AlCoCrFeNi_{2.1-x}Ni₃Al EHEA matrix composites exhibit higher hardness above 600 HV, which can be assumed to have better wear resistance. With the increase of Ni₃Al content, the hardness of AlCoCrFeNi_{2.1-x}Ni₃Al

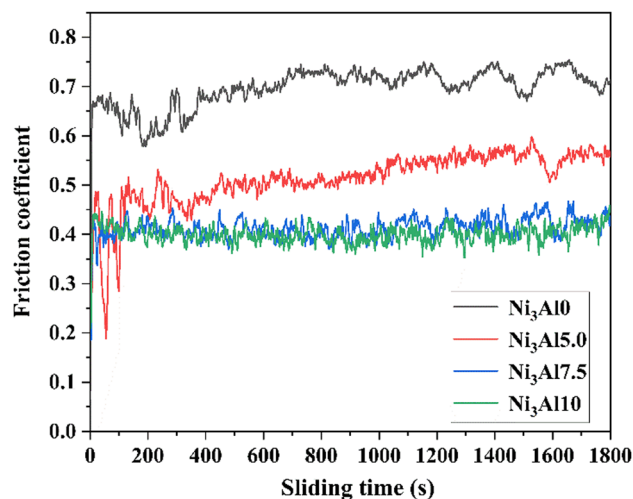


Fig. 5 Friction coefficient curves of the AlCoCrFeNi_{2.1-x}Ni₃Al EHEA matrix composites

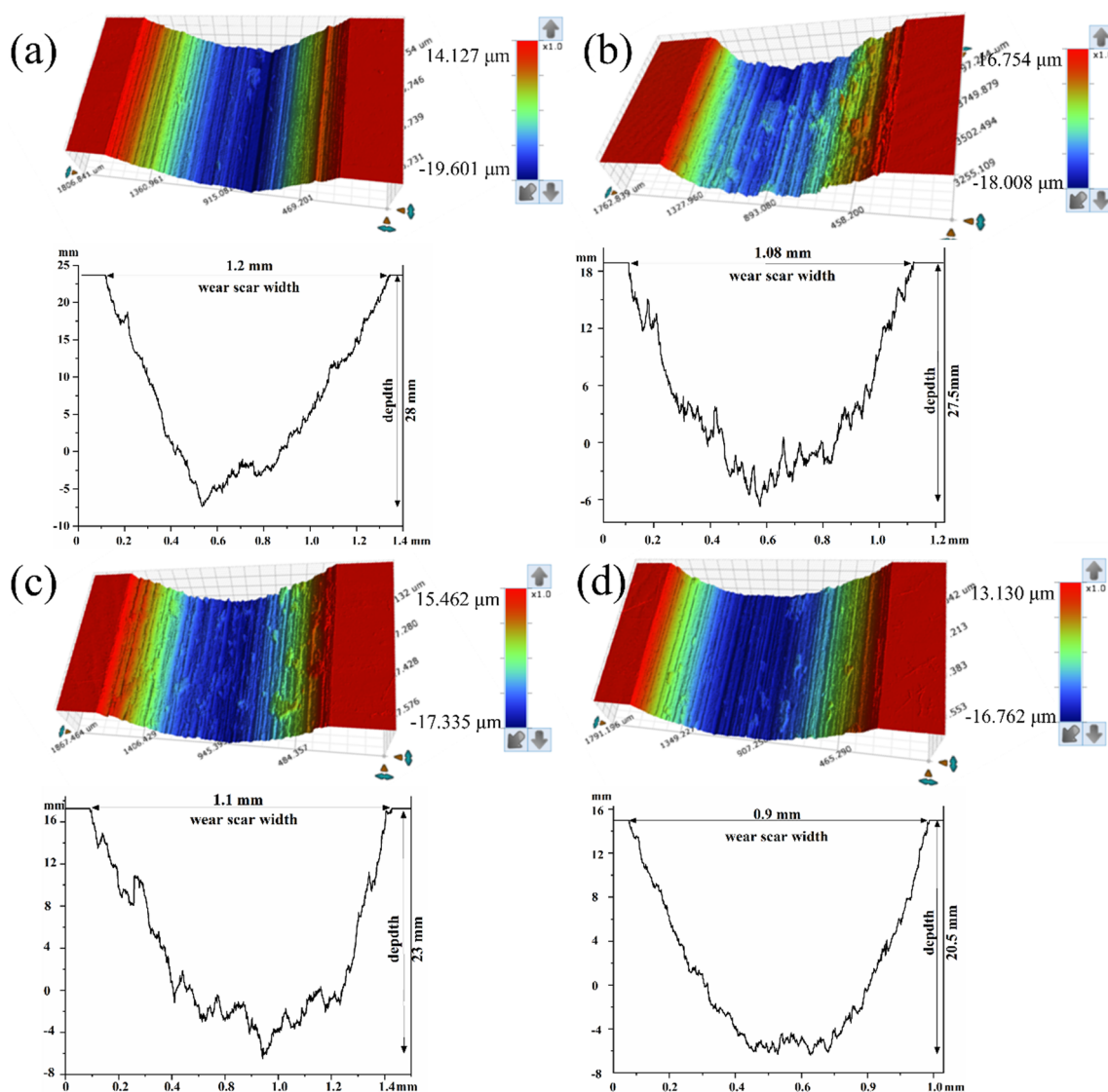


Fig. 6. 3D morphology and cross-section profiles of wear scar at middle part of the AlCoCrFeNi_{2.1-x}Ni₃Al EHEA matrix composites: **a** $x=0$, **b** $x=5.0$, **c** $x=7.5$, **d** $x=10$

composites shows a trend of decreasing from 629 HV ($x=0$) to 615 HV ($x=5.0$), and then gradually increasing from 615 HV to 626 HV ($x=10$). From the Fig. 4b, it can be found that the fracture occurs without significant yield in the AlCoCrFeNi_{2.1} alloy without the Ni₃Al. However, the addition of Ni₃Al significantly improves the plasticity of the AlCoCrFeNi_{2.1} alloy. With the increase of the Ni₃Al content, the compressive yield strength and compressive strain of AlCoCrFeNi_{2.1-x}Ni₃Al EHEA matrix composites gradually increase. The compressive fracture strength first increased, then decreased and finally increased significantly. Wherein, Ni₃Al10 composite exhibits excellent comprehensive mechanical properties, the compressive yield strength, the compressive fracture strength, compressive strain, and Vickers hardness are 1845 MPa, 2301 MPa, 10.1%, and 626

HV, respectively. The excellent mechanical properties may be resulted from the balance of the high hardness phase and the high plasticity phase in Ni₃Al10 composite. Meanwhile, the double-scale morphology may play a very important role for mechanical property [33, 34].

The friction coefficient is a basic parameter of the friction system, and the magnitude of the friction coefficient directly reflects the wear resistant property of the material. The friction coefficient of the AlCoCrFeNi_{2.1-x}Ni₃Al alloys is obtained, as illustrated in Fig. 5. The average friction coefficients of the AlCoCrFeNi_{2.1-x}Ni₃Al ($x=0$, 5.0, 7.5, 10 wt%) composites are 0.72, 0.5, 0.41, and 0.40, respectively. With the Ni₃Al content increasing from 0 to 10 wt%, friction coefficients of AlCoCrFeNi_{2.1-x}Ni₃Al composites shows a decreasing trend, especially the

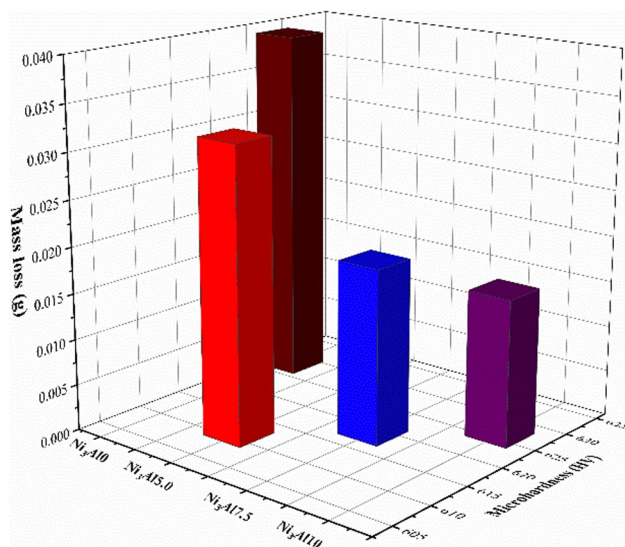


Fig. 7 Relation between mass loss and microhardness for the composites

friction coefficient of Ni₃Al10 composites reaches a minimum of 0.40. It can be seen that the friction coefficient of the AlCoCrFeNi_{2.1-x}Ni₃Al composites with Ni₃Al particle added is lower than that of the AlCoCrFeNi_{2.1} matrix without Ni₃Al particle under the same conditions. Which indicated that the addition of Ni₃Al can obviously enhance the wear resistant. Among them, the Ni₃Al10 alloy shows the lower friction coefficients and the least fluctuations, so it exhibits the best friction behavior.

Figure 6 shows the 3D morphologies and wear section profile of the worn surface of the AlCoCrFeNi_{2.1-x}Ni₃Al EHEA matrix composites. There are many grooves formed by micro-plowing on the worn surface of AlCoCrFeNi_{2.1-x}Ni₃Al composites, and the micro-plowing phenomenon is first increases and then gradually decreases with the addition of Ni₃Al. The width and depth of wear scar on the AlCoCrFeNi_{2.1-x}Ni₃Al composites with Ni₃Al particle added are narrower and shallower (see Fig. 6b–d) than those of AlCoCrFeNi_{2.1} matrix without Ni₃Al particle. Wherein, the Ni₃Al10 composite has the narrowest and shallowest wear tracks, which again proves that the Ni₃Al10 composite has the best wear resistance.

Figure 7 presents the relation between mass loss and microhardness for the AlCoCrFeNi_{2.1-x}Ni₃Al EHEA matrix composites. With the increase of Ni₃Al content, the mass loss gradually decreases, followed by 0.039 g, 0.032 g, 0.019 g and 0.016 g, respectively. According to Archard's law [35], the wear resistance of the material is positively related to hardness but high hardness will also increase the brittleness of the material, causing the wear resistance to decrease instead [36]. It can be seen that the Ni₃Al10 composite having the highest hardness

value exhibits the high mass loss, which may due to the high hardness of the composite increases the brittleness. However, the mass loss of the Ni₃Al5.0, Ni₃Al7.5 and Ni₃Al10 composites gradually decreases, which is positively related to hardness. The decreased mass loss of the composites may be resulted from the Ni₃Al particles added into the AlCoCrFeNi_{2.1} leading to the plasticity increased significantly, avoiding the extension of the cracks. This comparison indicates that Ni₃Al10 composite exhibits the best wear resistance, possibly owing to the optimal ratio of B₂+Cr₇C₃/Al₂O₃ hard phases and ductile L₁₂+FCC phases for about 1:1.

In order to further analyze the wear mechanism, the SEM images of worn surface of the AlCoCrFeNi_{2.1-x}Ni₃Al EHEA matrix composites are given in Fig. 8. It can be seen that the wear morphology of the Ni₃Al0 matrix is relatively rough (as shown in Fig. 8a), indicating severe wear occurs on the surface. The furrow morphology existed on the Ni₃Al0 matrix wear surface, which indicates the occurrence of abrasive wear. In addition, it can be seen from Fig. 8b that a large number of black smooth dense layers (see area A) appear on the wear surface of the Ni₃Al0 matrix. The EDS analysis reveals that the black dense layers contain high O element content, indicating that the area A is mainly oxide. It can be inferred that the oxidation reaction occurred on the wear surface, which is generated by the frictional heat generated during friction. Whereas some of the black oxide dense layer is accompanied by micro cracks, as shown in the top right corner of Fig. 8b. The area A with higher hardness reduces the contact area between the counterpart ball and sample surface resulting in the friction process is unstable. Which will cause stress concentration on the sample surface [37], leading to the cracks sprouting and expansion (see Fig. 9a). Then further grow, connect, and propagate along the microcracks as the friction and wear process continue (Fig. 9b). Finally, the mass materials of the surface are removed (see Fig. 9c), which leads to the high friction coefficient and mass loss of Ni₃Al0 matrix. In short, the main mechanism of Ni₃Al0 matrix is oxidation wear accompanied by slight abrasive wear.

On the surface of the Ni₃Al5.0 composite exhibits the general characteristics of the toughness deformation of the soft material wear surface along the sliding direction (see Fig. 8c), which is due to the sudden increase of plasticity and the hardness reduction with the addition of Ni₃Al. As well as the wear surface retains a small amount of O-enriched dense friction layer (see Fig. 8d). Thus, the main mechanism of

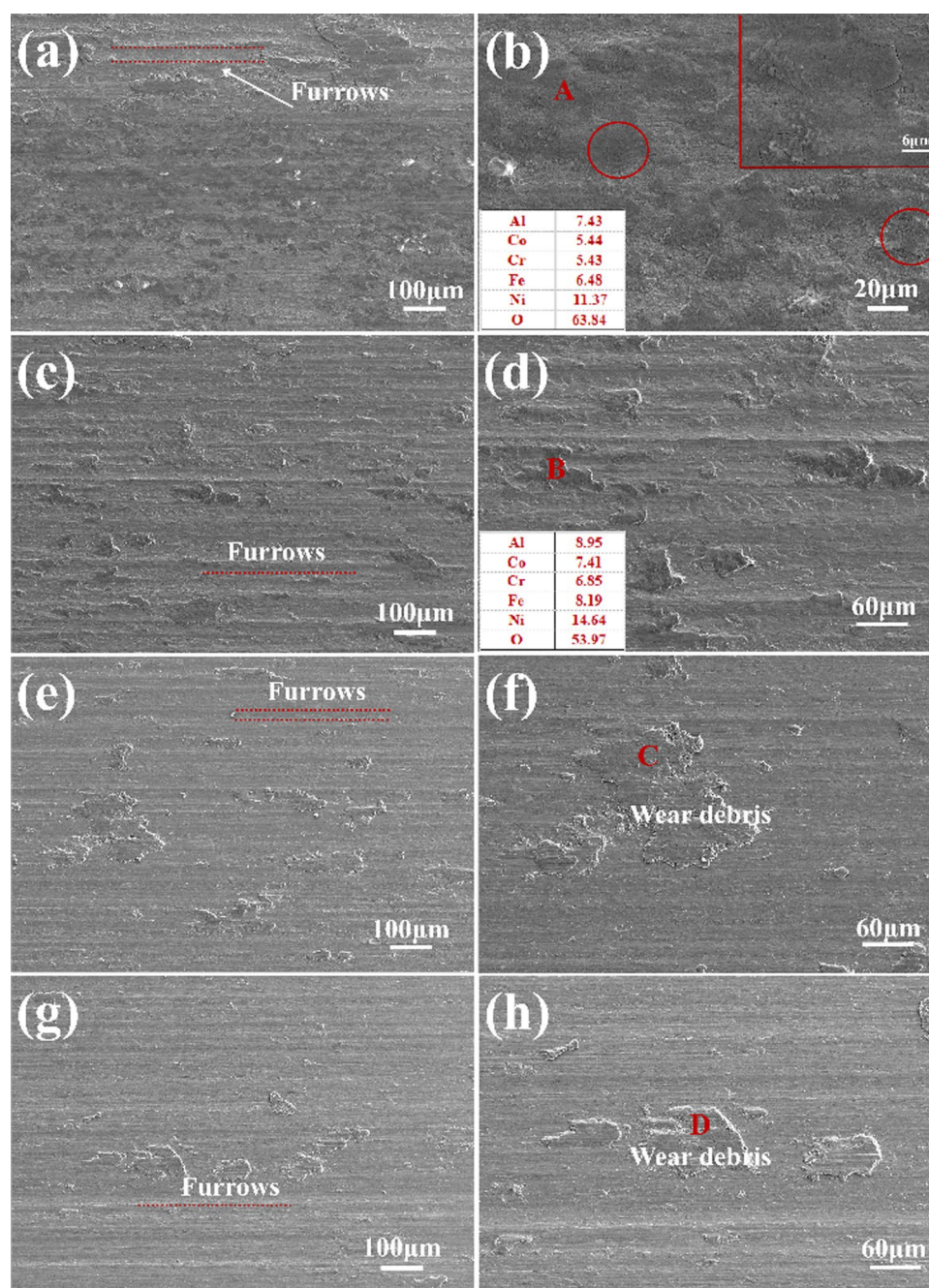


Fig. 8 SEM images of AlCoCrFeNi_{2.1-x}Ni₃Al EHEA matrix composites after wear: **a** and **b** $x=0$, **c** and **d** $x=5.0$, **e** and **f** $x=7.5$, **g** and **h** $x=10$

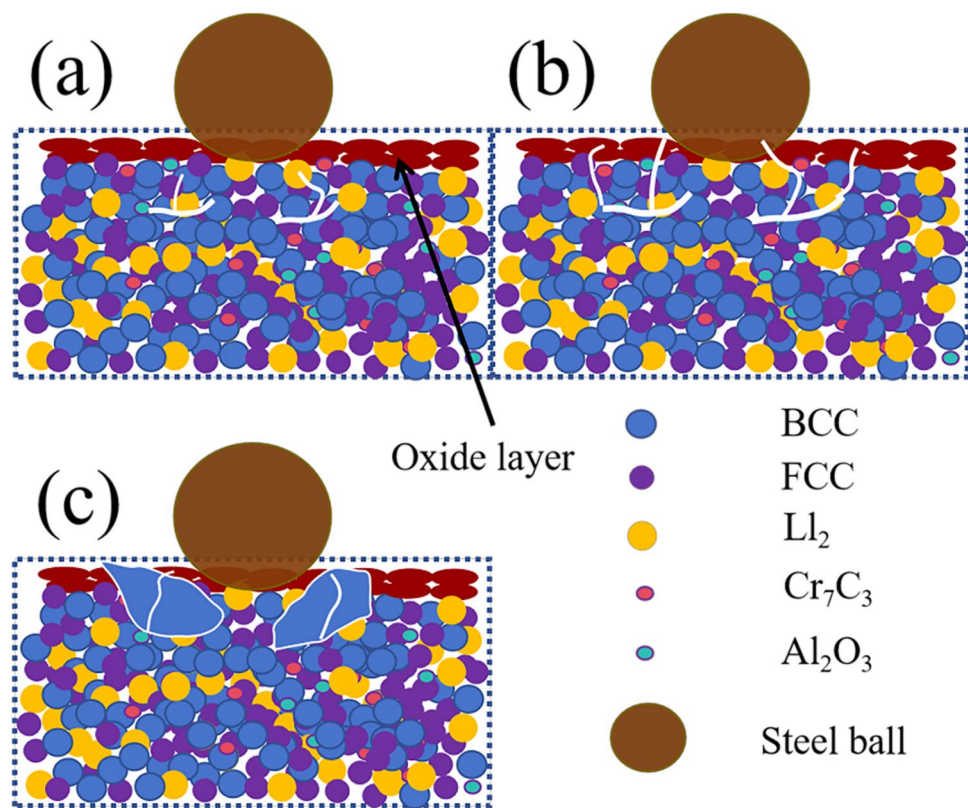


Fig. 9 a–c Schematic of microstructural evolution mechanism of “crack” phenomenon

Ni₃Al5.0 composite is abrasive wear accompanied by slight oxidation wear.

Unlike the previous worn surfaces, when the Ni₃Al content increases to 0.75 and 10, the wear surface changes smoothly with a few small adhered fragments and fine shallow furrows (see Fig. 8e–h), indicating that the wear resistance increases. During the friction process, the hard B2+Cr₇C₃/Al₂O₃ phases play a supporting role to avoid a lot of abrasive wear, while the soft Ll₂+FCC phases can prevent the brittle fracture of the alloy and reduces wear mass loss. Hence, the coupled interaction of the hard B2+Cr₇C₃/Al₂O₃ phases and the ductile Ll₂+FCC phases make the composites exhibit excellent wear resistance. In short, the main wear mechanism of Ni₃Al7.5 and Ni₃Al10 composites are adhesive and abrasive wear.

4 Conclusions

AlCoCrFeNi_{2.1-x}Ni₃Al ($x = 0, 5, 7.5, 10$ wt%) EHEA matrix composites were successfully prepared by powder metallurgy. The effects of Ni₃Al particle content on the microstructure, mechanical properties and wear resistance

of the AlCoCrFeNi_{2.1-x}Ni₃Al alloys were investigated. The main conclusions are as follows:

1. The AlCoCrFeNi_{2.1-x}Ni₃Al EHEA matrix composites present cellular grid microstructure composing of main FCC/Ll₂ and B2 phases, and a small amount of Al₂O₃ and Cr₇C₃ phases.
2. With the addition of Ni₃Al particles, compressive fracture strength, compressive yield strength and compressive strain of the AlCoCrFeNi_{2.1-x}Ni₃Al EHEA matrix composites enhance significantly. Wherein, the Ni₃Al10 alloy exhibit excellent comprehensive mechanical properties with the compressive yield strength of 1845 MPa, compressive fracture strength of 2301 MPa, and the compressive strain of the 10.1%.
3. The friction coefficient, wear width and depth, and mass loss of the AlCoCrFeNi_{2.1-x}Ni₃Al ($x > 0$) EHEA matrix composites were significantly lower than that of the AlCoCrFeNi_{2.1} alloy matrix under the same frictional wear conditions. Among them, the Ni₃Al10 alloy has the best wear performance, and the wear mechanism is main abrasive wear with a small amount of adhesive wear.

Acknowledgements This work was supported by the Support Program for Youth Innovation Technology in Colleges and Universities of Shandong Province (2023KJ095); the Qingdao Municipal Science and Technology Benefits the People Special Fund (24-1-8-cspz-3-nsh).

Declarations

Conflict of interest The authors state that there are no conflicts of interest to disclose.

References

- [1] V.N.V. Munagala, R. Richard, *Surf. Coat. Technol.* **411**, 126974 (2021)
- [2] Z.Y. Yang, J.Z. Fan, Y.Q. Liu, Y.L. Kang, J.H. Nie, *Mater. Sci. Eng.* **806**, 140804 (2021)
- [3] B. Gludovatz, A. Hohenwarter, D. Catoor, E.H. Chang, E.P. George, R.O. Ritchie, *Science* **6201**, 1153 (2014)
- [4] D.B. Miracle, O.N. Senkov, *Acta Mater.* **122**, 448 (2017)
- [5] A. Kilmametov, R. Kulagin, A. Mazilkin, S. Seils, T. Boll, M. Heilmaier, H. Hahn, *Scr. Mater.* **158**, 29 (2019)
- [6] Y.Z. Shi, B. Yang, X. Xie, J. Brechtel, K.A. Dahmen, P.K. Liaw, *Corros. Sci.* **19**, 33 (2017)
- [7] R. He, M. Wu, C. Cui, D.D. Jie, X.J. Miao, *J. Alloys Compd.* **970**, 172631 (2024)
- [8] S.R. Huang, H. Wu, Y.J. Chen, Z.G. Zhao, X.Y. Liu, Y.B. Deng, H.G. Zhu, *Compos. Commun.* **38**, 101510 (2023)
- [9] R.P. Wang, G. Wang, S.L. Ran, W. Wang, Y. Zhao, K.X. Gui, R.J. He, C.W. Tan, Y.L. Yang, *J. Eur. Ceram. Soc.* **43**, 1853 (2023)
- [10] H. Jiang, L. Li, J.M. Wang, C.B. Wei, Q. Zhang, C.J. Su, H.M. Sui, *Acta Metall. Sin. -Engl. Lett.* **36**, 987 (2023)
- [11] B.C. Liu, H.S. Chen, J. Zhou, W.X. Wang, S.X. Xi, X.C. Chen, *Vacuum* **217**, 112574 (2023)
- [12] D. Sun, Y.C. Cai, L.S. Zhu, F.F. Gao, M.D. Shan, S.S. Marwana Manladan, K.P. Geng, J. Han, Z.Y. Jiang, *Surf. Coat. Technol.* **438**, 128407 (2022)
- [13] B.P. Xu, Y.C. Zhou, Y.D. Liu, S.J. Hu, G.D. Zhang, *J. Mater. Res.* **37**, 1 (2022)
- [14] J.F. Zhang, T. Jia, H. Qiu, H.G. Zhu, Z.H. Xie, *J. Mater. Sci. Technol.* **42**, 122 (2020)
- [15] F.K. Zheng, G.N. Zhang, X.J. Chen, X. Yang, Z.C. Yang, Y. Li, J.T. Li, *Mater. Sci. Eng.* **774**, 138940 (2020)
- [16] Y.P. Lu, Y. Dong, S. Guo, L. Jiang, H.J. Kang, T.M. Wang, B. Wen, Z.J. Wang, J.C. Jie, Z.Q. Cao, H.H. Ruan, T.G. Li, *Sci. Rep.* **4**, 6200 (2014)
- [17] Y.P. Lu, Y. Dong, H. Jiang, Z.J. Wang, Z.Q. Cao, S. Guo, T.M. Wang, T.J. Li, P.K. Liaw, *Scr. Mater.* **187**, 202 (2020)
- [18] Y.P. Lu, X.Z. Gao, L. Jiang, Z.N. Chen, T.M. Wang, J.C. Jie, H.J. Kang, Y.B. Zhang, S. Guo, H.H. Ruan, Y.H. Zhao, Z.Q. Cao, T.J. Li, *Acta Mater.* **124**, 143 (2017)
- [19] H. Jiang, Z.L. Ni, J.M. Wang, D.X. Qiao, Y.T. Lv, G.S. Zhang, L. Liu, *Mater. Charact.* **201**, 112952 (2023)
- [20] J. Lu, H. Zhang, Y. Chen, L. Ling, X.Z. Liu, W.W. Xiao, N. Ni, X.F. Zhao, *Corros. Sci.* **180**, 109191 (2021)
- [21] J.M. Wang, H. Jiang, X.X. Chang, L.J. Zhang, H.X. Wang, L. Zhu, S.X. Qin, *Corros. Sci.* **221**, 111313 (2023)
- [22] M.H. Asoushe, A.Z. Hanzaki, H.R. Abedi, B. Mirshekari, T. Wegener, S.V. Sajadifar, T. Niendorf, *Mater. Sci. Eng. A* **799**, 140012 (2021)
- [23] W. Chen, Y.T. Wang, L.L. Wang, J.Q. Zhou, *Eng. Fract. Mech.* **246**, 107615 (2021)
- [24] J. Lu, H. Zhang, Y. Chen, L. Li, X.Z. Liu, W.W. Xiao, N. Ni, X.F. Zhao, F.W. Guo, P. Xiao, *Corros. Sci.* **180**, 109191 (2021)
- [25] I.S. Wani, T. Bhattacharjee, S. Sheikh, Y.P. Lu, S. Chatterjee, P.P. Bhattacharjee, S. Guo, N. Tsuji, *Mater. Res. Lett.* **4**, 174 (2016)
- [26] M.L. Wang, Y.P. Lu, T.M. Wang, C. Zhang, Z.Q. Cao, T.J. Li, P.K. Liaw, *Scr. Mater.* **204**, 114132 (2021)
- [27] M.L. Wang, Y.P. Lu, T.M. Wang, C. Zhang, Z.Q. Cao, T.J. Li, P.K. Liaw, *Acta Mater.* **248**, 118806 (2023)
- [28] Y. Yin, J.Q. Zhang, Q.Y. Tan, W. Zhuang, N. Mo, M. Birmingham, M.X. Zhang, *Mater. Des.* **162**, 24 (2019)
- [29] Y. Fu, J. Li, H. Luo, C.W. Du, X.G. Li, *J. Mater. Sci. Technol.* **80**, 217 (2021)
- [30] A. Liang, D.C. Goodelman, A.M. Hodge, F. Diana, S.P. Branicio, *Acta Mater.* **257**, 119163 (2023)
- [31] J.M. Wang, H. Jiang, W.L. Xie, X. Kong, S.X. Qin, H.W. Yao, Y. Li, *Corros. Sci.* **229**, 111879 (2024)
- [32] H. Ziaei, B. Sadeghi, Z. Marfavi, N. Ebrahimzadeh, P. Cavaliere, *Mater. Sci. Technol.* **36**, 604 (2020)
- [33] X. Zheng, W. Long, C.S. Zhu, L.B. Zhao, X.B. Hu, S. Liu, W.M. Jing, Y.S. Peng, *Materials* **17**, 182 (2023)
- [34] P. Jin, J.J. Zhou, J.X. Zhou, Y.B. Liu, Q.J. Sun, *Compos. Pt. B* **268**, 111078 (2024)
- [35] Y.F. Juan, J. Li, Y.Q. Jiang, W.L. Jia, Z.J. Lu, *Appl. Surf. Sci.* **465**, 700 (2019)
- [36] C.Y. Shang, E. Axinte, J. Sun, X.T. Li, P. Li, J.W. Du, P.C. Qiao, Y. Wang, *Mater. Des.* **117**, 193 (2017)
- [37] B. Bhushan, A. Banerjee, P.K. Bijalwan, S.N. Patel, A.N. Bhagat, S. Mandal, D. Banik, K. Mondal, *Surf. Coat. Technol.* **484**, 130765 (2024)

Springer Nature or its licensor (e.g. a society or other partner) holds exclusive rights to this article under a publishing agreement with the author(s) or other rightsholder(s); author self-archiving of the accepted manuscript version of this article is solely governed by the terms of such publishing agreement and applicable law.